A Practical Approach Toward Highly Reproducible and High-Quality Perovskite Films Based on an Aging Treatment

Yuqin Zou, Xinyu Bai, Simon Kahmann, Linjie Dai, Shuai Yuan, Shanshan Yin, Julian E. Heger, Matthias Schwartzkopf, Stephan V. Roth, Chun-Chao Chen, Jianping Zhang, Samuel D. Stranks, Richard H. Friend, and Peter Müller-Buschbaum*

Solution processing of hybrid perovskite semiconductors is a highly promising approach for the fabrication of cost-effective electronic and optoelectronic devices. However, challenges with this approach lie in overcoming the controllability of the perovskite film morphology and the reproducibility of device efficiencies. Here, a facile and practical aging treatment (AT) strategy is reported to modulate the perovskite crystal growth to produce sufficiently high-quality perovskite thin films with improved homogeneity and full-coverage morphology. The resulting AT-films exhibit fewer defects, faster charge carrier transfer/extraction, and suppressed non-radiative recombination compared with reference. The AT-devices achieve a noticeable improvement in the reproducibility, operational stability, and photovoltaic performance of devices, with the average efficiency increased by 16%. It also demonstrates the feasibility and scalability of AT strategy in optimizing the film morphology and device performance for other perovskite components including $MAPbI_3$, $(MAPbBr_3)_{15}(FAPbI_3)_{85}$, and $Cs_{0.05}(MAPbBr_3)_{0.17}(FAPbI_3)_{0.83}$. This method opens an effective avenue to improve the quality of perovskite films and photovoltaic devices in a scalable and reproducible manner.

1. Introduction

Metal halide-based hybrid perovskites have attracted widespread research and development interests due to their broad applicability and promising potential in photovoltaics,[1] light-emission diodes,[2] and photodetectors.[3] As a class of high-profile functional materials, perovskites exhibit not only remarkable electronic and optoelectronic properties[4] but also can be prepared with facile and low-cost solution-processing methods.[5] A wide range of deposition techniques, ranging from spin-coating, spray coating,[6] and printing[7] to vapor deposition,[8] have been used for the preparation of high-quality perovskite thin films. Among various methods, spin-coating, using anti-solvent treatment to facilitate the removal of the host solvent and initiate the crystallization of perovskite films, is a well-established and widely applied method.

Y. Zou, S. Yin, J. E. Heger, P. Müller-Buschbaum
Technical University of Munich
TUM School of Natural Sciences
Department of Physics
Chair for Functional Materials
James-Franck-Str. 1, 85748 Garching, Germany
E-mail: muellerb@ph.tum.de

X. Bai, L. Dai, S. D. Stranks, R. H. Friend
Department of Physics
Cavendish Laboratory
University of Cambridge
Cambridge CB3 0HE, UK

S. Kahmann, S. D. Stranks
Department of Chemical Engineering and Biotechnology
University of Cambridge
Cambridge CB3 0AS, UK

S. Yuan, J. Zhang
Department of Chemistry
Renmin University of China
No. 59 Zhongguancun Street, Beijing 100872, P. R. China

M. Schwartzkopf, S. V. Roth
Deutsches Elektronen-Synchrotron (DESY)
Notkestrasse 85, 22607 Hamburg, Germany

S. V. Roth
Department of Fibre and Polymer Technology
KTH Royal Institute of Technology
Teknikringen 56–58, Stockholm SE-100 44, Sweden

C.-C. Chen
School of Materials Science and Engineering
Shanghai Jiao Tong University
Shanghai 200240, P. R. China

P. Müller-Buschbaum
Heinz Maier-Leibnitz-Zentrum (MLZ)
Technical University of Munich
Lichtenbergstr. 1, 85748 Garching, Germany

**ADVANCED
SCIENCE NEWS**
www.advancedsciencenews.com

**ADVANCED
MATERIALS**
www.advmat.de

The efficiency and stability of perovskite solar cells (PSCs) are strongly dictated by the electronic properties and trap state density in the perovskite light-harvesting layer. In turn, the electronic properties and trap density are influenced by the film crystallization and morphology.[9] Early investigations on crystal growth implemented in situ techniques such as grazing-incidence wide-angle X-ray scattering (GIWAXS), photoluminescence (PL) spectroscopy, and optical absorbance, to elucidate the crystallization mechanisms, short-lived intermediates, or the structural transformation kinetics from solution to solid-state films.[9a,10] The physicochemical evolution of organic and inorganic perovskite film formation involves multiple steps: i) A rapid nucleation of polydisperse perovskite nanocrystals triggered by the anti-solvent drop; ii) the metastable intermediate phases in which solvent-complexes, non-perovskite or yellow δ phases, transform to crystalline perovskite upon thermal disassociation and solvent evaporation; iii) the formation of perovskite crystals in films after complete dissolving and recrystallizing.[9a,10a] Finely tuning the crystal crystallization kinetics, that is, the nucleation-growth process of perovskite films, is recognized as a desirable and effective strategy to achieve high-quality film with full-coverage, smoothness, and large-grained morphology.[9d,11] So far, several strategies such as flash infrared annealing,[12] vacuum flash-assisted solution processing,[13] and liquid medium annealing,[9d] have been developed to optimize the nucleation-growth process and eliminate undesirable structural constrains, leading to an advantageous film morphology. However, the imbalance between nucleation and growth rate during the film formation easily leads to undesirable situations such as forming perovskite films with dendritic structures, voids, or poor coverage.[11] In addition, the parameter variability of anti-solvent (volume, types, drip rate, drip time, and so on) in practical application strongly affects the material conversion pathways and leads to a variable and poorly reproducible film quality.[9b,14] Therefore, considering the strong correlation between device performance and film structural characteristics, significant efforts toward practical and controllable film processing technology are still required to meet the demands of scalable and reproducible fabrication.

Recently, many impressive outcomes have been achieved through the fine control and optimization of anti-solvent and annealing steps.[9b,d] In the present work, an inconspicuous aspect of the perovskite film formation is focused on, namely crystallization control between the anti-solvent step and the annealing step, which was reported by a previous work for its effect on film morphology and device performance.[15] Here, we find it has a dramatic effect on the MAPbI$_3$ (abbreviated as MAPI) perovskite film morphology and device performance by keeping the as-cast film at room temperature for 2 min in a nitrogen (N$_2$) atmosphere prior to annealing (called aging treatment, denoted as AT). The AT process well controls the removal of the residual host solvents N, N-dimethylformamide (DMF) and dimethyl sulfoxide (DMSO) to mitigate the interference of solvents on the crystal growth in subsequent annealing and prevent the volatile component loss from the desired stoichiometry, as well as initiate the initial growth of perovskite crystals. As a result, the AT-MAPI thin films have a full-coverage, homogeneity, and void-free morphology. The AT-MAPI devices exhibit superior charge carrier dynamics, enhanced average fill factor (FF), and power conversion efficiency (PCE) with high reproducibility, as well as improved

operational stability under vacuum and ambient conditions. Moreover, the influence of AT on (MAPbBr$_3$)$_{0.15}$(FAPbI$_3$)$_{0.85}$ (abbreviated as MAFA), Cs$_{0.05}$(MAPbBr$_3$)$_{0.17}$(FAPbI$_3$)$_{0.83}$ (abbreviated as CsMAFA), and (MAPbBr$_3$)$_{0.05}$(FAPbI$_3$)$_{0.95}$ (abbreviated as FAPI) perovskite components, as well as MA$_{1-x}$FA$_x$PbI$_3$ and MAPbI$_{1-x}$Br$_x$ families, is also systematically investigated to explore the working mechanism of AT and its applicability to other perovskite components.

2. Results and Discussion

2.1. Morphology, Crystal Structure, and Charge Carrier Dynamics of MAPI- and MAFA-Based Films

The perovskite film morphology is strongly affected by the perovskite component, spin-coating parameters, and annealing conditions. During the film preparation, an interesting phenomenon is found in the film morphology, as described schematically in **Figure 1**a. After spin-coating, the perovskite-coated substrates are aged at room temperature in an N$_2$-filled glovebox (steady-state atmosphere) before annealing at 100 °C. Here, we express this process as aging treatment, abbreviated as AT. The unaged and aged samples are referred to as Ref- and AT- in the following discussion, respectively. The directly annealed films exhibit a large cluster distribution with poor coverage. In contrast, the AT-thin films exhibit homogenous grain size and comprehensive coverage. Figure S1, Supporting Information shows the color variation occurring in the perovskite films aged at room temperature in an N$_2$-filled glovebox for different times, as well as the front and back sides of the annealed perovskite films. As the aging time increases (Figure S1a, Supporting Information), the color of unannealed films gradually changes from transparent for an unaged film to yellow for the 8 min aged film, implying that part of the intermediate species converts into perovskite or non-perovskite phases. Further, with the prolongation of the aging time, the appearance of the annealed films changes from whitish for unaged films to bright black for aged films from the front and back sides of the films (Figure S1b,c, Supporting Information). Figure S2, Supporting Information shows the current density–voltage (J–V) curves of the champion devices aged at different times. The detailed photovoltaic parameters are listed in Table S1, Supporting Information. The J–V data are extracted from the same batch. The highest PCE is achieved in the devices aged for 2 min at room temperature, with a PCE of 18%, a J_{SC} of 20.07 mA cm^{-2}, a V_{OC} of 1.12 V, and an FF of 0.73. However, the longer aging time has little effect on the film morphology and device performance. Therefore, in the following discussion, the AT refers to the film being aged at room temperature in an N$_2$-filled glovebox for 2 min. Scanning electron microscopy (SEM) (Figure 1b) reveals that the well-defined micro-scale clusters formed in the Ref-MAPI film by direct annealing transform into pinhole-free nano-scale grains with the AT process, accompanied by substantially better film coverage. The substantial variation in the grain size is reflected in the film thickness, which decreases from 389 to 329 nm for the AT-MAPI film (Figure S3a, Supporting Information). Likewise, atomic force microscopy (AFM) measurements reveal (Figure 1c) a considerably decreased surface root mean square (RMS) roughness, from 70.9 nm for Ref-MAPI to 17.3 nm for AT-MAPI, suggesting a reduced height difference
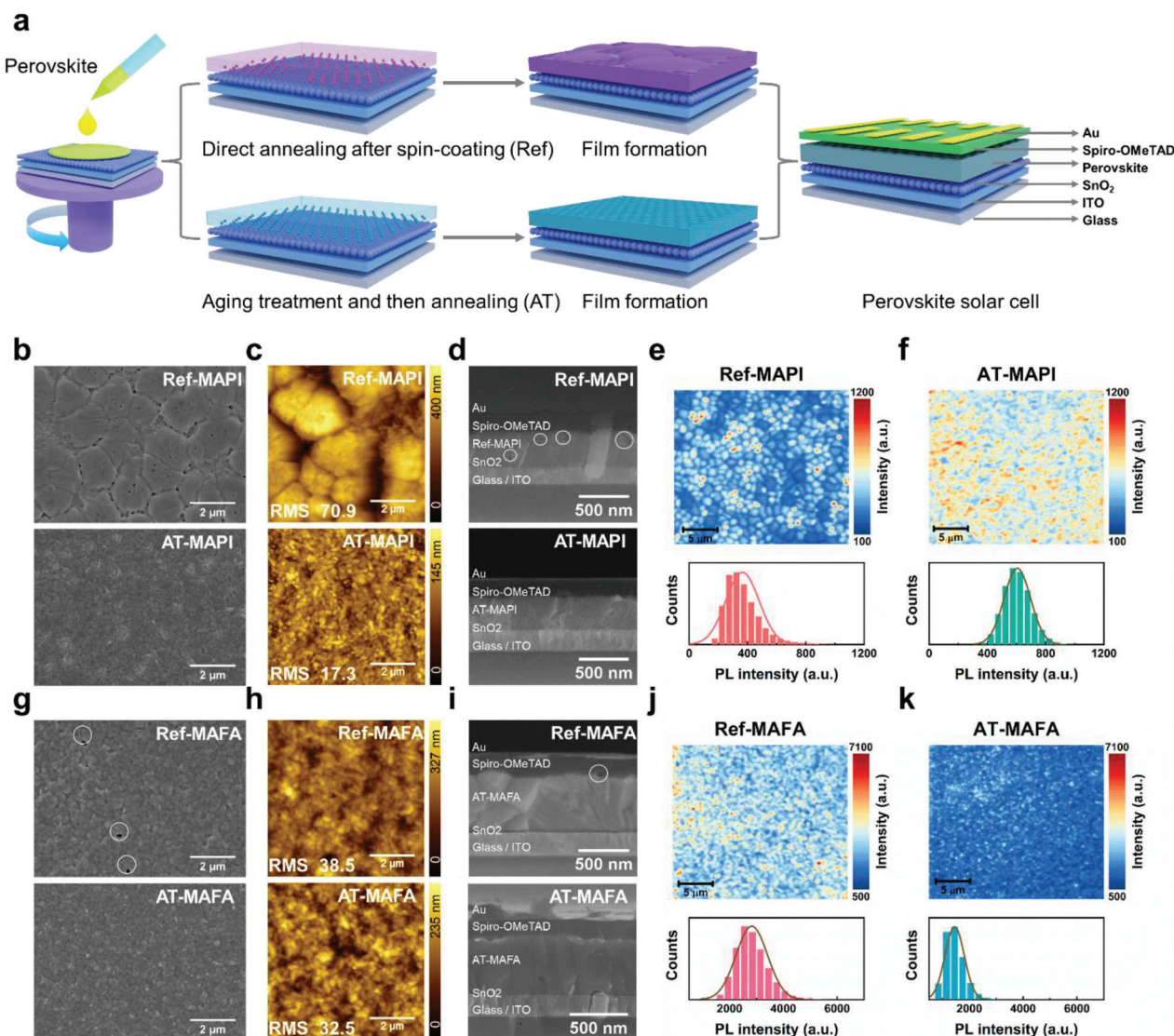
Figure 1. a) Schematic illustration of the Ref process (top row) and the AT process (bottom row) for film and device fabrication. Top-view SEM images of the Ref- and AT-thin films with a scale bar of 2 µm. b) MAPI, g) MAFA. AFM images of the Ref- and AT-thin films with a scale bar of 2 µm. c) MAPI, h) MAFA. Cross-section SEM images of the Ref- and AT-devices with a scale bar of 500 nm. d) MAPI, i) MAFA, based on glass/ITO/SnO$_2$/perovskite/spiro-OMeTAD/Au. Time-resolved photoluminescence mapping of perovskite films with the PL intensity as the target signal (top) and the intensity distribution (bottom). e) Ref-MAPI, f) AT-MAPI, j) Ref-MAFA, and k) AT-MAFA. The solid black line is the fitting to the distribution curve. Perovskite thin films on quartz are encapsulated with glass slides and epoxy. Samples are photoexcited with a 405 nm laser through a 100 × 0.9 NA air objective at a fluence of 4 µJ cm^{-2} per pulse.

between grains. The cross-sectional SEM images of Ref- and AT-MAPI devices (Figure 1d) show monolithic grains from top to bottom. However, a few voids (white circles) are observed in the perovskite layer of Ref-MAPI device.

The difference in the perovskite thin film morphology is also reflected in the optical properties of thin films. Fluorescence intensity maps are collected over a 25 × 25 µm^2 region of the perovskite thin films on quartz substrates (Figure 1e,f, top). The MAPI samples are photoexcited at 405 nm at 4 µJ cm^{-2} per pulse and a repetition rate of 2 MHz. We extract the histogram of the PL intensity from the maps (Figure 1e,f, bottom). The respective mean and standard deviation values are listed in Table S2, Supporting Information. The PL intensity distribution of AT-MAPI

film is narrowed, with a standard deviation of 91. In contrast, the Ref-MAPI film exhibits a much broader distribution with a standard deviation of 115. This narrower intensity distribution of the AT-MAPI film suggests a better homogeneity than the Ref-MAPI film. We also notice that the PL intensity of the AT-MAPI film (mean value ≈ 605 a.u.; Figure 1f, bottom) is significantly higher than that of the Ref-MAPI films (mean value ≈ 365 a.u.; Figure 1e, bottom) under the same photoexcitation conditions. This finding suggests that the AT process has a positive effect on the photoluminescence properties of the MAPI perovskite in addition to improving the thin film homogeneity.

When the AT process is applied to the MAFA component, we do not observe discernible differences in the grain sizes of the

2307024 (3 of 14)

**ADVANCED
SCIENCE NEWS**

www.advancedsciencenews.com

**ADVANCED
MATERIALS**

www.advmat.de

Ref- and AT- thin films as in the case of MAPI, but some voids are still visible at the grain boundaries of the Ref-MAFA film, unlike the full-coverage and well-developed crystallites seen in the AT-MAFA film (Figure 1g, white circle). The poor coverage of the perovskite film on the hole blocking layer (HBL) surface of the Ref-MAPI and MAFA components leads to electrical contacts between the electron blocking layer (EBL) and HBL deposited on the top and bottom of the active layer, forming an electrical short that lowers the voltage of the PSCs.[16] Similar to MAPI, the surface roughness of the AT-MAFA film decreases from 38.5 to 32.5 nm (Figure 1h) and no voids are observed in the AT-MAFA device from the cross-sectional SEM images (Figure 1i, white circle). We also measure the PL intensity mapping of the Ref- and AT-MAFA films in a 25×25 µm^2 area (Figure 1j,k, top). Consistent with the more uniform film morphology, the AT-MAFA film also shows a relatively narrower PL intensity distribution (standard deviation of 360 a.u.; Figure 1k, bottom) than the Ref-MAFA film (standard deviation of 587 a.u.; Figure 1j, bottom), together with a lower PL intensity. The reduction in PL intensity does not significantly affect the device performance, but the better film uniformity contributes to its photovoltaic efficiency, as discussed in the following device performance section. In the X-ray diffraction (XRD) spectra (Figure S4, Supporting Information), the weakened PbI$_2$ phase and the disappeared yellow δ-phase FAPbI$_3$ located at 11.6° in AT-MAPI and MAFA films suggest that the AT process suppresses the generation of PbI$_2$ and non-perovskite phases. These findings highlight the positive effects of the AT on the morphology and crystal structure of perovskite films.

We further measure grazing-incidence wide-angle X-ray (GIWAXS) scattering to gain information about the crystallite structure and preferential crystallite orientation by probing reciprocal lattice distances inside the Ref- and AT-thin films and analyzing the azimuthal intensity distribution of the scattered intensity. 2D GIWAXS data transformed to q-space (reshape) is shown in **Figure 2**a,b, where q is the scattering vector. The presence of a Debye–Scherrer ring with an isotropic intensity distribution indicates a completely random crystal orientation; while, the sharp and distinct Bragg spots suggest that the films have a highly preferential crystal orientation. According to this, the 2D GIWAXS data of all samples show diffraction signals at all angles, implying multiple crystal orientations. To obtain detailed information about the phase orientation, we perform an azimuthal tube cut along the (110) Debye–Scherrer ring (Figure 2a,b, white ring) of the 2D GIWAXS data and analyze it with a Gaussian profile fit. To better visualize the crystal orientation, a pseudo-cubic perovskite lattice illustration with cubic-shaped crystallites is provided (Figure 2c,d, inset). As shown in Figure S5a, Supporting Information, both Ref- and AT-MAPI films adopt a preferential face-on orientation at around $\chi = 0°$ (red and green area), which corresponds to the (110) plane of MAPI crystals oriented parallel to the substrate surface (Figure 2c, inset). In both samples, partial crystallites are isotopically distributed along all angles (grey area). Despite the fact that huge differences are observed in the film morphology (Figure 1b,g), the crystal orientations of the Ref- and AT-MAPI thin films are similar. The GIWAXS data also indicate that the large crystal domain observed in the Ref-MAPI film comprises multiple smaller crystallites rather than a complete single-crystal structure because the scattering signal in the

2D GIWAXS data is a diffraction ring with a smeared intensity distribution. Unlike MAPI, the Ref- and AT-MAFA films show two higher order diffraction signals at around $\chi = 36°$ and 68° (Figure S5b, Supporting Information), indicating a preferential crystal growth with an edge-on orientation, which means that the (001)/(110) planes of the MAFA crystals are tilted by 36° or 68° with respect to the substrate surface (Figure 2d, inset).

Next, we calculate the true material quantity (MQ) to get an insight into the crystal orientation distribution. The signal intensity is Lorentz-corrected by multiplying with sin χ to be converted to a pole figure presentation of the line cuts from the 2D GIWAXS data (Lorentz-corrected I [χ] × sin χ versus χ plots in Figure 2c,d).[17] The MQ is directly accessible for face-on, edge-on and isotropic crystal orientation by integrating the areas under the respective curve in the pole figures. The calculated results are shown in Figure 2e,f, where the face-on, edge-on, and isotropic MQs are shaded with different colors. For the AT-MAPI film (Figure 2e), the relative MQ$_{iso}$ (MQ$_{rel}$ = MQ/MQ$_{tot}$, with MQ$_{tot}$ = ΣMQ, of the respective orientation: face-on, edge-on and isotropic[17]) of the isotropic orientation decreases from 89% to 82%, and correspondingly, the MQ$_{face}$ increases from 11% to 18%. Interestingly, the isotropic orientation MQ$_{iso}$ of the Ref-MAFA film accounts for 16% of the total crystallites and increases to 52% with the AT process, accompanied with the MQ$_{edge}$ decreasing from 84% to 48% (Figure 2f). The relative MQ results indicate that the AT process promotes the MAPI crystallites to stack in face-on orientation to some extent; while, the MAFA crystallites are preferentially oriented isotropically. Whether the effect of AT on the phase orientation is related to the perovskite component will be further verified in the study of CsMAFA and FAPI materials.

Subsequently, transient absorption (TA) measurements are performed to investigate the influence of AT on charge carrier dynamics. We follow the charge carrier dynamics at the band edge to investigate charge carrier recombination in the perovskite films at low charge carrier density (Figure 2g–h). TA kinetics of the ground state bleaches are acquired under a 400 nm pump at fluences of 3.14 µJ cm^{-2} per pulse (Figures S6 and S7, Supporting Information). We extract the monomolecular non-radiative recombination coefficient k_1 by fits to the tail of the GSB kinetics with a monoexponential equation (Figure 2i,j). Fits to different time domains of the TA kinetics are conducted to verify the reliability of k_1. The fits to the TA curves are displayed in Figure S8, Supporting Information, and the corresponding extracted k_1 values are listed in Table S3, Supporting Information. The k_1 values extracted from the TA for the AT-MAPI film are ≈four times lower than those without AT; while, the change in the MAFA sample signals is not significant. It suggests that the AT process could suppress the non-radiative recombination in the MAPI component but has no apparent effect on the MAFA component.

2.2. Photovoltaic Performance and Operational Stability of MAPI- and MAFA-Based PSCs

Based on the above discussion, we find that the AT process has a positive effect on achieving uniform thin films. Herein, we proceed to investigate the effect of the AT on the
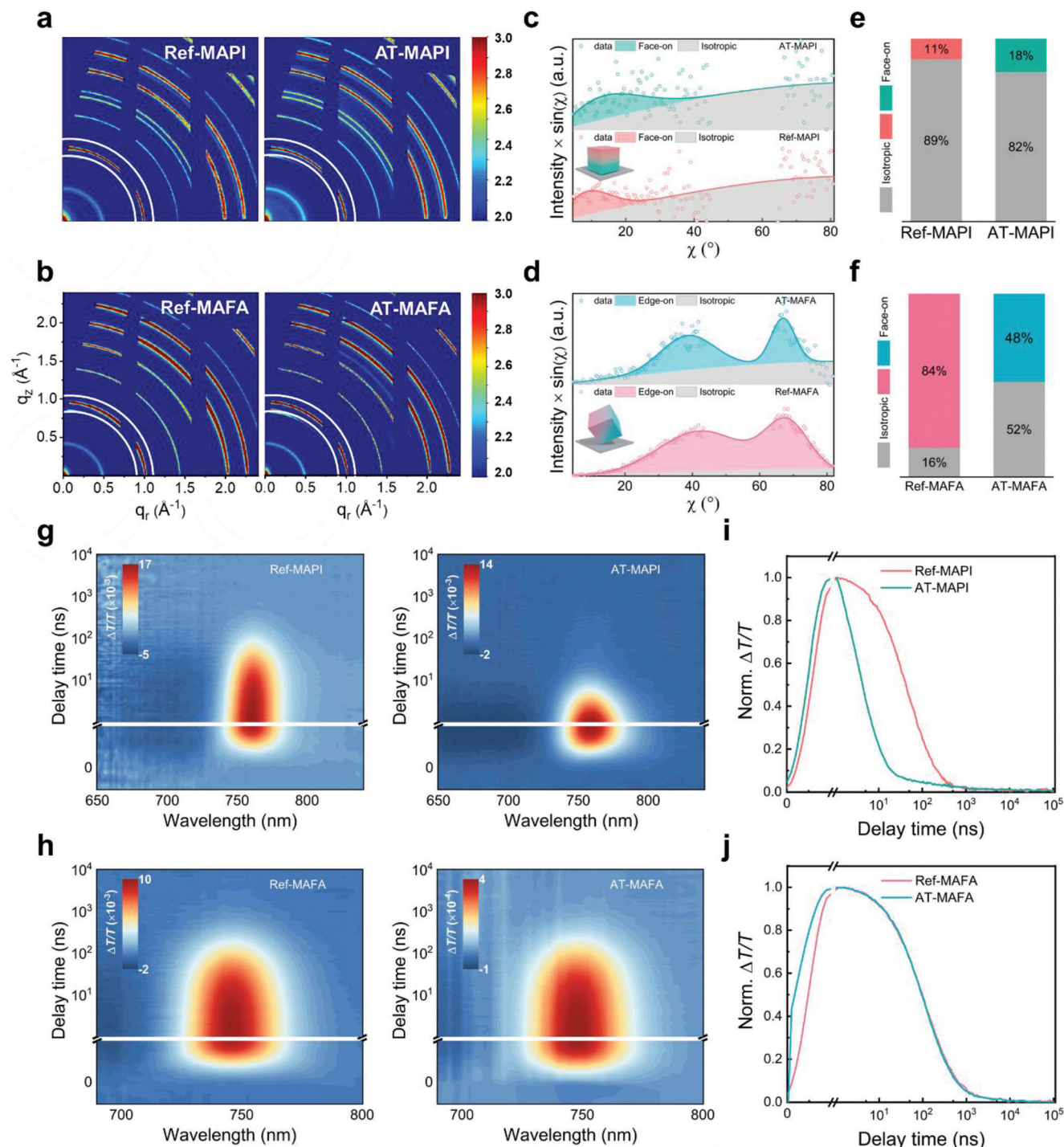
Figure 2. 2D GIWAXS data of Ref- and AT-thin films. a) MAPI, b) MAFA. Pole figure representation of the Ref- and AT-thin films obtained through azimuthal tube cuts along the (002)/(110) Bragg peak around $q = 1.00$ Å^{-1} of 2D GIWAXS data measured at $\alpha_i = 0.60°$. c) MAPI, d) MAFA, with different color areas corresponding to the edge-on, face-on, and isotropic material quantity MQ, respectively. The edge-on and face-on orientations are illustrated by 3D model cubes (inset). The relative material quantity (MQ) of each orientation. e) MAPI, f) MAFA. Transient absorption (TA) color maps of the Ref- and AT-thin films. g) Ref- and AT-MAPI, h) Ref- and AT-MAFA thin films. Kinetics at the ground state bleaches (GSB). i) MAPI, j) MAFA thin films extracted from (g,h). Samples are photoexcited at 400 nm at the repetition rate of 500 Hz. The fluence of the laser is ≈3.14 µJ cm^{-2} per pulse. All the samples are encapsulated with glass slides and epoxy to protect them from degradation during the TA measurements.

2307024 (5 of 14)
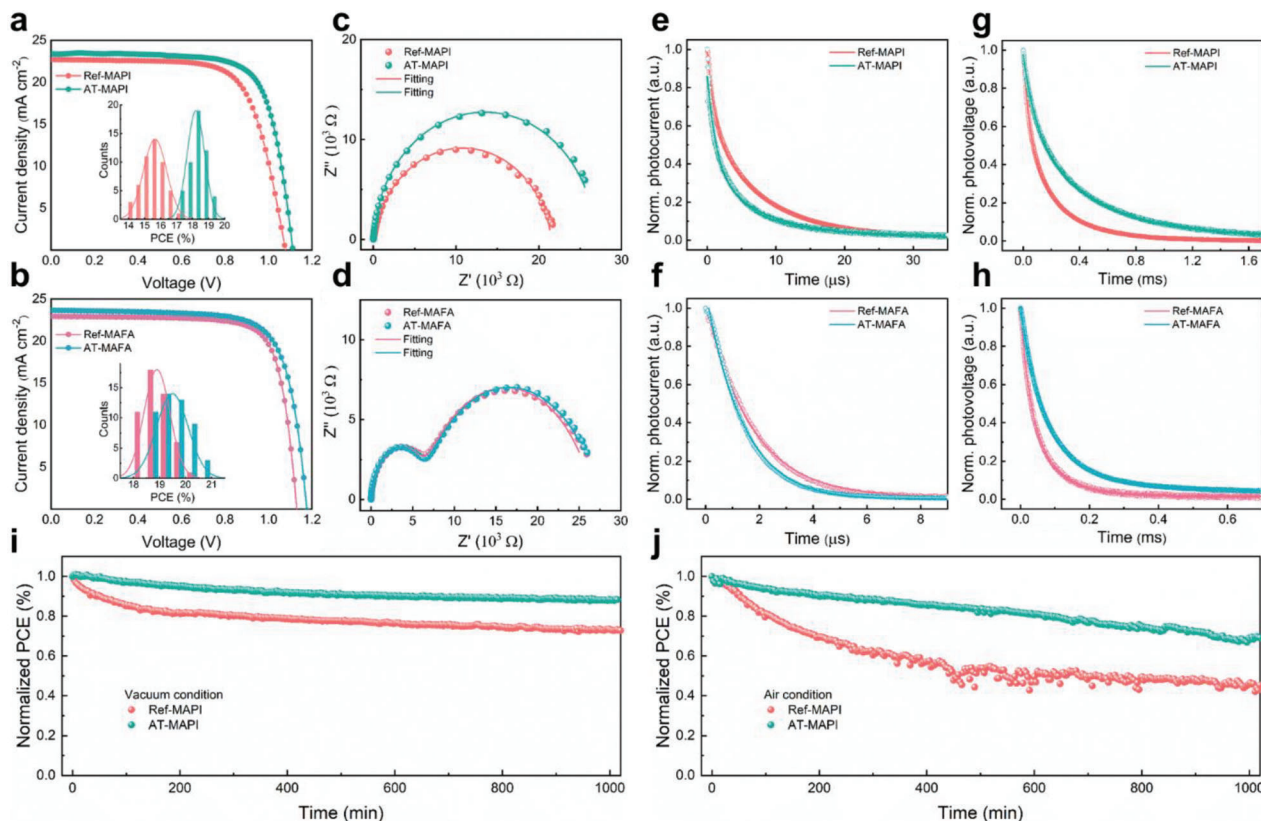
Figure 3. J–V curves of the champion devices measured under simulated AM 1.5G sunlight. a) MAPI, b) MAFA; inserted is the statistical distribution of PCE based on 50 cells from different batches. Nyquist plots of EIS of the Ref- and AT-devices. c) MAPI, d) MAFA. Transient photocurrent traces of the Ref- and AT-devices. e) MAPI, f) MAFA. Transient photovoltage traces of the Ref- and AT-devices. g) MAPI, h) MAFA. Operational stability of un-encapsulated devices under continuous AM 1.5G illumination. i) vacuum condition, j) air condition.

photovoltaic performance and charge carrier kinetics in MAPI- and MAFA-devices, with planar device structure consisting of glass/ITO/SnO$_2$/perovskite/spiro-OMeTAD/Au. **Figure 3**a,b shows the J–V curves of the champion MAPI and MAFA devices and the PCE statistical distribution based on 50 cells from different batches, respectively. The statistical distributions of other device parameters are shown in Figures S9 and S10, Supporting Information. The detailed photovoltaic parameters are summarized in Table S4, Supporting Information. The highest PCE of MAPI-based PSCs increases from 17.3% for the Ref-device to 19.3% for the AT-device with FF increasing from 0.71 to 0.75. With the application of the AT process, the average PCE increases by 16%, together with a noticeably improved average FF (from 0.69 to 0.76) and V_{OC} (from 1.02 to 1.06 V). In the case of MAFA, the highest PCE increases from 20.1% for the Ref-device to 20.8% for the AT-device with the V_{OC} increasing from 1.13 to 1.17 V. Accordingly, the average PCE of the AT-MAFA devices increases by 3% and the average V_{OC} increases from 1.14 to 1.15 V. To further investigate the difference between homogeneity and reproducibility improvements of optoelectronic properties, we collect the J–V data of 20 MAPI- and MAFA-based cells from the same batch and plot the statistical distributions in Figures S11 and S12, Supporting Information, with the corresponding photovoltaic parameters listed in Table S5, Supporting Information. It shows similar results in the performance optimization with that from different

batches. Looking at the J–V data, we find that the main contribution of the AT to the photovoltaic performance lies in the increase of V_{OC} and FF, which is consistent with the SEM results that less V_{OC} loss can be achieved in full-coverage films by avoiding direct contact between HBL and EBL.[16] Although the Ref-films have thicker active layers and higher absorption capability, the poor coverage and inhomogeneity of the perovskite films could lead to V_{OC} and J_{SC} loss (Figures S3 and S13, Supporting Information). Besides, the AT-devices deliver excellent reproducibility with a narrow PCE distribution (Figure 3a,b, inset). Moreover, the dark J–V curves (Figure S14, Supporting Information) indicate that the AT process increases the parallel resistance by suppressing pinhole formation, suggesting that the Ref-MAPI device suffers from higher series resistance, which then translates to a lower FF.

To gain more insights into the effect of the film morphology on the interfacial charge carrier transfer and recombination kinetics, we perform electrochemical impedance spectroscopy (EIS) measurements under dark condition (Figure 3c,d) and analyze the Nyquist plots with an equivalent circuit model (Figure S15, Supporting Information); the fitting parameters are listed in Table S6, Supporting Information. The smaller R_{tr} (71.3 and 12.3 Ω for Ref- and AT-MAPI, 5.7 and 5.7 kΩ for Ref- and AT-MAFA) and the larger R_{rec} (21.5 and 26.9 kΩ for Ref- and AT-MAPI, 21.1 and 21.8 kΩ for Ref- and AT-MAFA) values in AT-MAPI and

ADVANCED
SCIENCE NEWS
www.advancedsciencenews.com

**ADVANCED
MATERIALS**
www.advmat.de

MAFA devices indicate more efficient charge carrier transfer at the interface and suppressed interface recombination, which is in agreement with the higher average V_{OC} and FF achieved in the $J–V$ data.[18] Transient photocurrent decay (TPC) and transient photovoltage decay (TPV) measurements are implemented under short-circuit and open-circuit conditions, respectively, to further investigate the charge carrier dynamics within the device.[19] Figure 3e,f shows the TPC traces, with the extracted transport lifetime τ_t listed in Table S7, Supporting Information. The τ_t decreases from 4.38 μs for the Ref-MAPI device to 2.34 μs for the AT-MAPI device and from 1.82 μs for the Ref-MAFA device to 1.48 μs for the AT-MAFA device. The shorter τ_t suggests a more efficient charge carrier transfer process from the perovskite layer to the charge blocking layer in the AT-devices.[19,20] In the TPV measurement (Figure 3g,h; Table S8, Supporting Information), the substantially longer charge carrier recombination lifetime τ_r (increases from 0.12 ms for the Ref-MAPI device to 0.28 ms for the AT-MAPI device, from 0.05 ms for the Ref-device to 0.09 ms for the AT-MAFA device) represents a reduced trap density in the perovskite layer and suppressed charge carrier recombination.[20,21] The enhanced charge carrier collection efficiency explains well the higher average V_{OC} achieved in the AT-devices (Table S4, Supporting Information).[22] We find that the crystal stacking pattern is not the dominant factor in determining the optoelectronic properties of the perovskite films and resulting devices.[23] Instead, achieving full-coverage voids-free perovskite films with less defects within the bulk and at the interface of perovskite films is more critical for high-efficiency PSCs.

Besides the absolute performance, device stability is also important. In general, the perovskite films with poor coverage provide more moisture and oxygen infiltration channels, thereby accelerating the perovskite component degradation.[24] Thus, to investigate whether the AT application influences the stability of the fabricated devices, we monitor the photovoltaic performance of non-encapsulated PSCs under vacuum and air conditions at room temperature, respectively. The normalized PCE data of MAPI devices are plotted in Figure 3i,j, with other parameters plotted in Figure S16, Supporting Information. As shown in Figure 3i, the AT-MAPI device maintains 88% of its initial efficiency after continuous operation for 17 h under standard AM 1.5G illumination under vacuum condition; while, the Ref-MAPI device rapidly degrades to 73% of its initial value. Under air condition, the AT-MAPI device retains 70% of its original efficiency after operating for 17 h, whereas the Ref-MAPI device decreases to 44% (Figure 3j). The slight increase in the PCE of the AT-MAPI device at the beginning of operation arises from the light-induced defect healing in the perovskite active layer.[21] In the case of MAFA devices, the AT-MAFA devices show a slight improvement in operational stability under both conditions (Figure S17, Supporting Information). The stability measurements suggest that the AT process could potentially enhance the device stability by optimizing the film morphology.

2.3. Morphology, Crystal Structure, and Photovoltaic Performance of Ref- and AT-MA$_{1-x}$FA$_x$PI Films and Devices

From the above discussion, we find that the AT process has a minor influence on the MAFA component but strongly affects the MAPI film morphology and the respective device performance. The main difference between the MAPI and MAFA components is their FA and Br content. Therefore, we continue to explore the correlation between the AT process and the FA and Br content using MAPI as a reference, respectively. **Figure 4**a,b and Figure S18, Supporting Information depict the morphology variation of Ref- and AT-MAPI films doped with different FA ratios (denoted as MA$_{1-x}$FA$_x$PI). From the macroscopic appearance (Figure 4a,b, inset, top right), with the AT process, the whitish Ref-films are transformed into black and translucent films. Besides, the incorporation of FA mitigates the degree of whitening (Figure 4a). From the perspective of microscopic morphology, increasing the ratio of FA in the MAPI component will decrease the cluster size in the Ref-films but can't avoid the formation of voids (Figure 4a, white circle). In contrast, the AT-MA$_{1-x}$FA$_x$PI thin films show a dense and uniform morphology besides weakening the effect of FA content (Figure 4b). These findings re-emphasize the role of AT process in improving the film coverage and preventing void formation. Likewise, the dramatic disparity is also reflected in the film thickness (Figures S19a–e and S20a,b and Table S9, Supporting Information). With the FA incorporation ratio increasing, the thickness of the AT-MA$_{1-x}$FA$_x$PI thin films increases from 329 to 398 nm; while, that of the Ref-MA$_{1-x}$FA$_x$PI thin films is maintained around 400 nm. This observation indicates that direct annealing induces the formation of thicker films; while, the incorporation of FA minimizes the thickness difference between Ref- and AT-thin films. As the x increases from 0.0 to 0.3, the gradual red shift (from 780 to 820 nm; Figure S21a,b, Supporting Information) of the absorption onset and the movement (from 14.10° to 14.02°; Figure S22a–d, Supporting Information) of the diffraction peaks towards lower angles indicate the formation of a mixed MA$_{1-x}$FA$_x$PI phase.[25] A tailing phenomenon, possibly related to grain size, is observed in the absorption beyond the band-gap in the Ref-MA$_{1-x}$FA$_x$PI films and gradually weakens with increasing FA ratio (Figure S23a–e, Supporting Information, red circle).[25] Notably, the diminishing until vanishing PbI$_2$ phase in Ref- and AT-MA$_{1-x}$FA$_x$PI films suggests a reduced loss of organic components with the AT process and the incorporation of FA (Figure S24a–e, red circle).

Figure 4c,d shows the Lorentz-corrected pole-figures of line cuts from the 2D GIWAXS data of Ref- and AT-MA$_{1-x}$FA$_x$PI films, with the related 2D GIWAXS data shown in Figure S25a,b, Supporting Information. Both types of MA$_{1-x}$FA$_x$PI thin films show a strong scattering signal at $\chi = 0°$, suggesting that the crystals are stacked along the face-on direction. As the FA ratio increases, the preferential face-on orientation transforms into an isotropic orientation. Figure 4e shows the fraction of the face-on and isotopically oriented crystallites calculated by integrating the areas of the corresponding features in the pole figures. The face-on orientation MQ$_{rel}$ decreases from 11% to 0% for the Ref-MA$_{1-x}$FA$_x$PI thin films and from 18% to 2% for the AT-MA$_{1-x}$FA$_x$PI thin films. For the AT-MA$_{1-x}$FA$_x$PI thin films doped with different FA ratios, the MQ$_{rel}$ of face-on orientation is higher than that of the Ref-MA$_{1-x}$FA$_x$PI thin films. In terms of the fraction of crystalline orientations, we find that the incorporation of FA induces the crystals to grow from a well-ordered face-on orientation to an isotropic stacked structure; while, more crystallites prefer to grow along the face-on direction during the AT process.

2307024 (7 of 14)
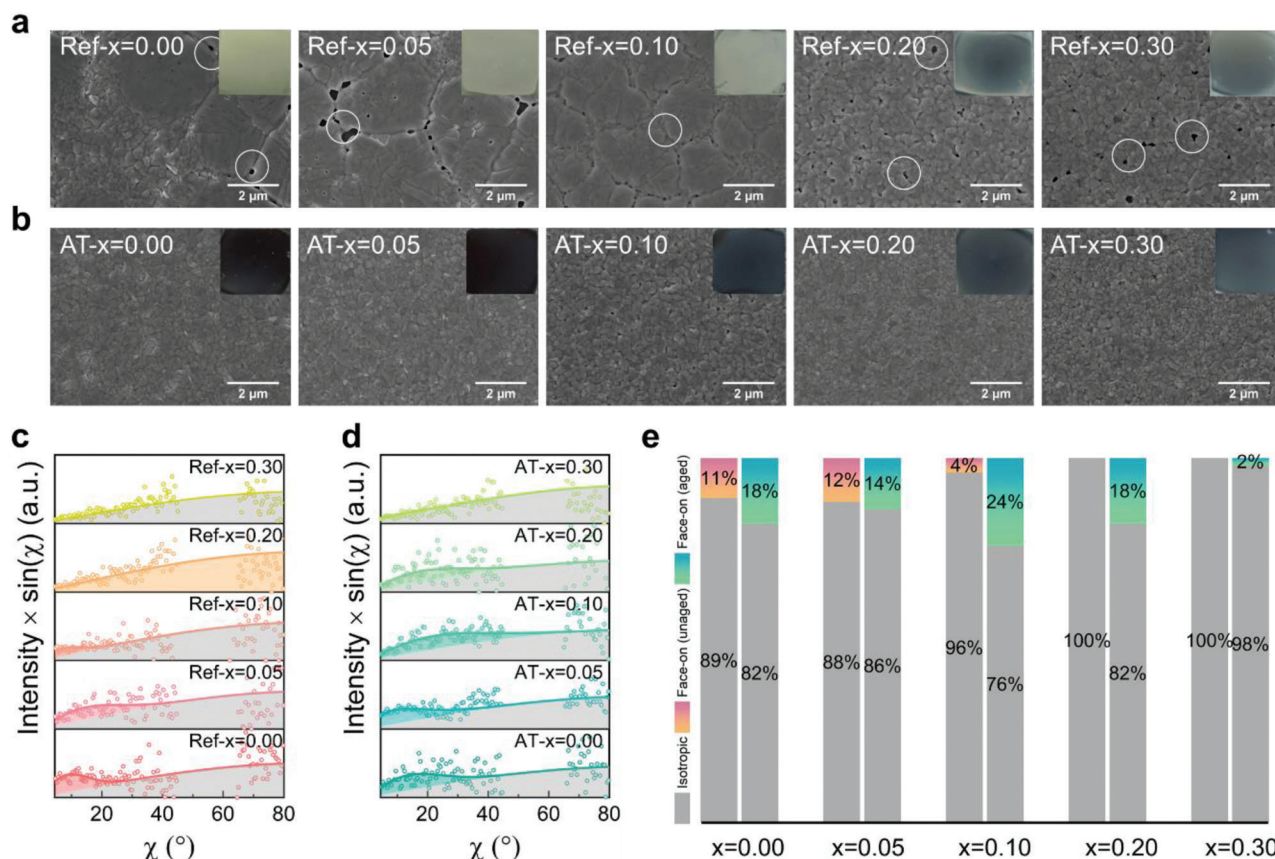
Figure 4. Top-view SEM images of perovskite films with a scale bar of 2 μm. a) Ref-$MA_{1-x}FA_xPI$, b) AT-$MA_{1-x}FA_xPI$. Pole figure representation. c) Ref-$MA_{1-x}FA_xPI$, d) AT-$MA_{1-x}FA_xPI$, through azimuthal tube cuts along the (002)/(110) Bragg peak around $q = 1.00$ Å^{-1} of 2D GIWAXS data measured at $\alpha_i = 0.60°$. Areas painted with different colors correspond to isotropic and face-on material quantity MQ, respectively. e) Relative material quantity MQ_{rel} of face-on and isotropically oriented crystallites based on (002)/(110) Bragg peak.

The photovoltaic performance of Ref- and AT-$MA_{1-x}FA_xPI$ devices is also investigated. Figure S26a–d, Supporting Information shows the statistical distribution of the related photovoltaic parameters for Ref- and AT-$MA_{1-x}FA_xPI$ devices (based on 20 devices from the same batch), with the detailed parameters summarized in Table S10, Supporting Information. As seen, the main contribution of AT to the performance improvement of $MA_{1-x}FA_xPI$ device still originates from the improved V_{OC} and FF values. Notably, the difference between the photovoltaic parameters of Ref- and AT-$MA_{1-x}FA_xPI$ devices gradually narrows as x increases from 0.0 to 0.3. This finding agrees with the film morphology variation observed in SEM (Figure 4a,b), suggesting an intrinsic correlation between film morphology and device performance. We attribute the noticeable improvement in the photovoltaic properties again to the formation of full-coverage and pinhole-free films that avoid the voltage loss arising from the electrical contact between HBL and EBL through voids.[16]

2.4. Morphology and Crystal Structure of Ref- and AT-MAPI$_{1-x}$Br$_x$ Films

We further investigate the effect of Br content on the morphology and crystal structure of MAPI films. Figure S27a,b, Supporting

Information shows the SEM images of Ref- and AT-MAPI thin films doped with different Br ratios (denoted as MAPI$_{1-x}$Br$_x$). The SEM images of Ref-MAPI$_{1-x}$Br$_x$ thin films show that the incorporation of Br has similar effects to FA, preventing the cluster coalescence of nanoparticles but voids remain (Figure S27a, Supporting Information, white circles). As x increases from 0.0 to 0.3, the large isolated domain structure is transformed into small-sized crystals, forming dense and homogeneous films with the AT process. In addition, the grain size of the AT-MAPI$_{1-x}$Br$_x$ thin films gradually becomes larger with the increase of the Br ratio (Figure S27b, Supporting Information), which is in agreement with previous reports.[26] Similar to FA, we also observe tailing behavior in the UV–vis spectra of Ref-MAPI$_{1-x}$Br$_x$ thin films (Figure S28a–e, Supporting Information, red circle). When x increases from 0.0 to 0.3, the energy band-gap (E_g) widening induced by the composition regulation leads to a systematic blue-shift (from 780 to 710 nm) in the absorption band-edge of both types of films (Figure S29a,b, Supporting Information).[27] Moreover, the characteristic peaks of the perovskite shift toward higher 2θ values (from 14.10° to 14.32° for [110] planes) due to the gradual substitution of larger I atoms by smaller Br atoms (Figure S30a–d, Supporting Information).[27] These results suggest the formation of a mixed MAPI$_x$Br$_{1-x}$ perovskite phase. In addition, the weakened PbI$_2$ phase reaffirms the inhibitory effect of AT

**ADVANCED
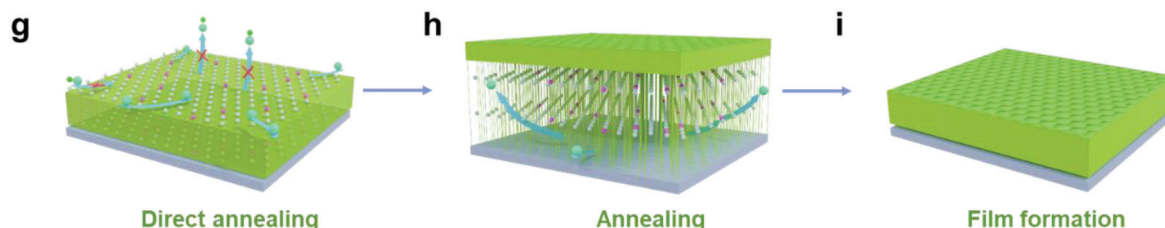SCIENCE NEWS**

www.advancedsciencenews.com

**ADVANCED
MATERIALS**

www.advmat.de
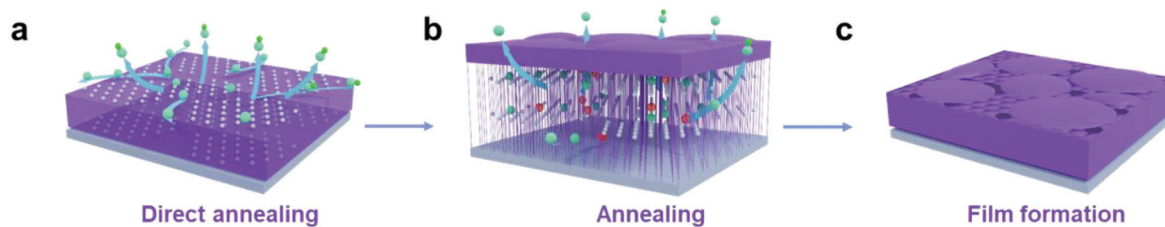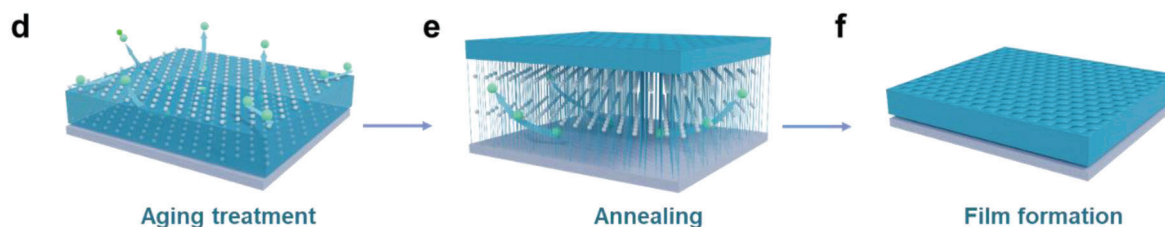
Figure 5. Schematic diagram of the perovskite film formation process under different conditions. a–c) MAPI component without AT. d–f) MAPI component with AT. g–i) Perovskite component incorporated with FA, Br, or Cs elements.

and Br on the generation of impurity phase PbI_2 (Figure S31a–e, Supporting Information, XRD, red circle). Figures S32a,b and S33a,b, Supporting Information show the 2D GIWAXS data and the Lorentz-corrected orientation distribution of (110) Bragg peak of the Ref- and AT-MAPI$_x$Br$_{1-x}$ films, respectively. A pronounced increased intensity at $\chi = 0°$ appears in all films, suggesting a preferential face-on orientation. According to the correction between the face-on and isotropic MQ and the Br ratios (Figure S33c, Supporting Information), we find that the incorporation of Br could increase the probability of Ref-MAPI$_x$Br$_{1-x}$ crystals growing along the face-on direction (from 11% to 26% as x increases from 0.0 to 0.3); while, the AT could weaken the preferred face-on orientation at each doping ratio of Br, decreasing from 14% to 11% for $x = 0.05$, from 23% to 14% for $x = 0.10$, from 26% to 24% for $x = 0.20$, and from 26% to 21% for $x = 0.30$.

2.5. Mechanisms of AT, FA, and Br Affecting Film Morphology

The crystal aggregation forms isolated domains surrounded by numerous pinholes, probably originating from the film dewetting during formation. During spin-coating, dynamic anti-solvent dripping leads to rapid structural change within the precursor phase; metastable nucleated phase converts into crystalline solvent-complex MAPI-DMSO or other intermediate phases.[10a] With thermal annealing, the intermediate phase undergoes further structural transition and converts into crystalline perovskite by thermal disassociation and subsequent solvent evaporation.[9a] Literature reports that solvent evaporation rates develop a vertical gradient from the film–air interface to the film–substrates interface.[28] The residual solvent leaves the surface first by evaporation and takes longer to escape from the bulk. Thus, the conversion of the intermediate phase to perovskite starts from the top surface of wet films; and then, crystallizes downward until being fully converted.[28b] When the wet MAPI films are immediately exposed to thermal condition, the thermal annealing drives the residual solvent at the air surface to rapidly evaporate and lift the diffusion confinement of nucleated species via overcoming the energy barrier.[9a,29] A different initial temperature on the air-surface of wet films leads to a horizontal difference in the solvent evaporation rate, from the periphery to the center, forming different degrees of solvent evaporation flow (**Figure 5**a). This difference disrupts the distribution of nucleated species or causes cluster coalescence of the nanoparticles. In addition, the thermal annealing, as well as the solvent evaporation and diffusion, can lead to MA loss because of the volatility and good solubility in the solvent; which, results in a decrease in the density of metastable nuclei MAI-DMSO. The dual

**ADVANCED
SCIENCE NEWS**

www.advancedsciencenews.com

**ADVANCED
MATERIALS**

www.advmat.de

effects of the solvent evaporation and the loss of organic components lead to decreased density and spatially inhomogeneous distribution of the metastable intermediate phase (Figure 5a). The crystals start to grow and form grains with different sizes due to space constraints (Figure 5b). It is found that the grains with smaller radius tend to be dissolved more easily because of their comparatively higher chemical potential and are adsorbed by the larger grains with lower chemical potential through Ostwald ripening.[11,29] This behavior drives the mass transportation between grains and the coarsening of large perovskite grains until the evaporation of the residual solvent in the intermediates is terminated (Figure 5b). As a result, in the case of inhomogeneous distribution of nucleated species, films without fully impinged large-sized perovskite domains are generated, manifesting as the perovskite film doesn't completely cover the substrates and contains many voids (Figure 5c). Some voids observed from cross-sectional SEM should originate from the volume shrinkage caused by the conversion and crystallization of perovskite or the space left by the residual solvent evaporation or other volatile species during direct annealing (Figure 1d,i).[15c,28b]

It is found that the intermediate phase at the top surface rapidly converted into the perovskite phase within 3 s annealing.[28b] Even at room temperature, the conversion and crystallization of the perovskite phase are already initiated after spin-coating.[30] Here, we believe that the AT plays two roles. One role is to reserve time for the removal of residual solvent from the film-air surface and shallow bulk (Figure 5d). The solvent diffusion during aging is no longer affected by thermal driving, allowing the precursor elements to inter-diffuse slowly.[11,26,30a] This process alleviates the interference on the distribution of nucleated species and the loss of volatile organic cation MA^+ caused by the rapid solvent evaporation flow during direct annealing. The reduced loss of organic component MA is confirmed by the weakened PbI_2 peak in the XRD data of Ref- and AT-perovskite films (Figures S4, S24, and S31, Supporting Information). The second role of the AT is that during aging, the intermediate phase starts to transform and initiates growth as the removal of residual solvent from the top surface, creating a crust of crystallized perovskite on the film surface (Figure 5e).[9a,28b,31] We observe that the almost translucent wet film gradually changes to light yellow during the AT (Figure 1a), indicating that part of the intermediate species is converted into perovskite or non-perovskite phase. In this state, both intermediate and perovskite phases coexist. In the subsequent thermal annealing, the film undergoes a rapid structural transition as solvent molecules escape from the bulk and achieves the perovskite grains coarsening via dissolution–recrystallization (Figure 5f). Therefore, the AT process initiates the phase transformation and completes the initial grain growth, which protects the volatile components from escaping and avoids the clustering of the sol–gel colloids because of the heterogeneous solvent removal. Besides, the AT process provides a buffer against the collapse of the as-cast film into isolated domains and allows the formation of uniform, continuous, and pinhole-free film morphology.

With the incorporation of FA into the MAPI component, we find significant differences in the film morphology and surface coverage depending on the ratio of MA and FA. The isolated domains, poor coverage, and void-containing film gradually transform into homogenous films. Such differences can be minimized by replacing the volatile A-site cation MA with more thermally stable cation FA, leading to better thermal stability of the as-cast film.[9c] Under thermal annealing, the loss of organic cations is decreased, thereby mitigating the effect on the density of nucleating species (Figure 5g). This finding is confirmed by the gradually weakened until vanished PbI_2 phase in the XRD data of $MA_{1-x}FA_x$PI films (Figure S24, Supporting Information, red circle). In addition, it was found that MAI retains more solvent in the film and leaves some solvent in a volatile state as the solution is transformed into as-cast state, which slows down the solvent loss during spin-coating and delays the crystallization of the perovskite phase.[10] In the FA-dominated component (MAFA, CsMAFA, FAPI), the yellow δ phase (2H), non-perovskite phase (4H), and desirable perovskite phase (3C) are simultaneously formed upon anti-solvent dripping, and the former two get converted into 3C perovskite phase during thermal annealing, rather than solvate phase.[10a] Thus, the substitution of MA by FA lowers the amount of residual solvent in the as-cast film and improves the crystallization rate before thermal annealing, which is important to alleviate the impact of solvent outflow and evaporation on the film morphology (Figure 5h). The variation in the film morphology (Figures 1b,g and 4a,b) is consistent with previous reports that the thermal conversion of as-cast films occurs in a "liquid" state that contains a high solvent volume fraction, yielding films with poor morphology.[10]

In the $MAPI_{1-x}Br_x$ component, the Pb—Br bonds are stronger than the Pb-DMSO bonds as opposed to the Pb—I bonds being weaker than the Pb—DMSO bonds.[10a,32] The difference in the lead–solvent interactions in the presence of iodide and bromine reflects the solvent loss rate at room temperature or under thermal annealing conditions. The solvent molecules are hard to evaporate when preferentially complexed with iodide-bound lead and easily evaporate when interacting with bromide-bound lead.[10a] When Br is introduced to replace the I-sites, the solvent DMSO loss rate is faster because of the stronger Pb—Br bonds than the Pb—DMSO bonds, leading to a lower solvent volume fraction. The preferential loss of solvent in the Br-containing component quickly creates a supersaturation state, which promotes the nucleation and growth of intermediate phases. This supersaturation state is crucial for the subsequent rapid thermal transition from non-perovskite phase to the desirable 3C perovskite phase. In addition, more solvent is extracted with the anti-solvent dropping in the Br-containing component, which weakens the interference of solvent evaporation on the crystallization process during the thermal annealing. When Cs^+ is added into the perovskite component, the almost no obvious difference in the film morphology (Figure S34a, Supporting Information) originates from the formation of 3C perovskite phase, 2H, and 3H phases upon anti-solvent dripping, which is less affected by the residual solvent. Previous studies indicated that the addition of Cs^+ lowers the energy barrier for forming the perovskite phase, which facilitates the formation of an entropically stabilized perovskite phase even at room temperature.[33] Moreover, it was found that the incorporation of FA^+, Br^-, and Cs^+ could improve the thermal stability and extend the longevity of the sol–gel state, even after the onset of crystallization.[10a] This could provide a buffer to prevent the as-cast film from collapsing into isolated domains. Instead, they form full-coverage, highly crystalline, and pinhole-free films (Figure 5i). This description also explains why
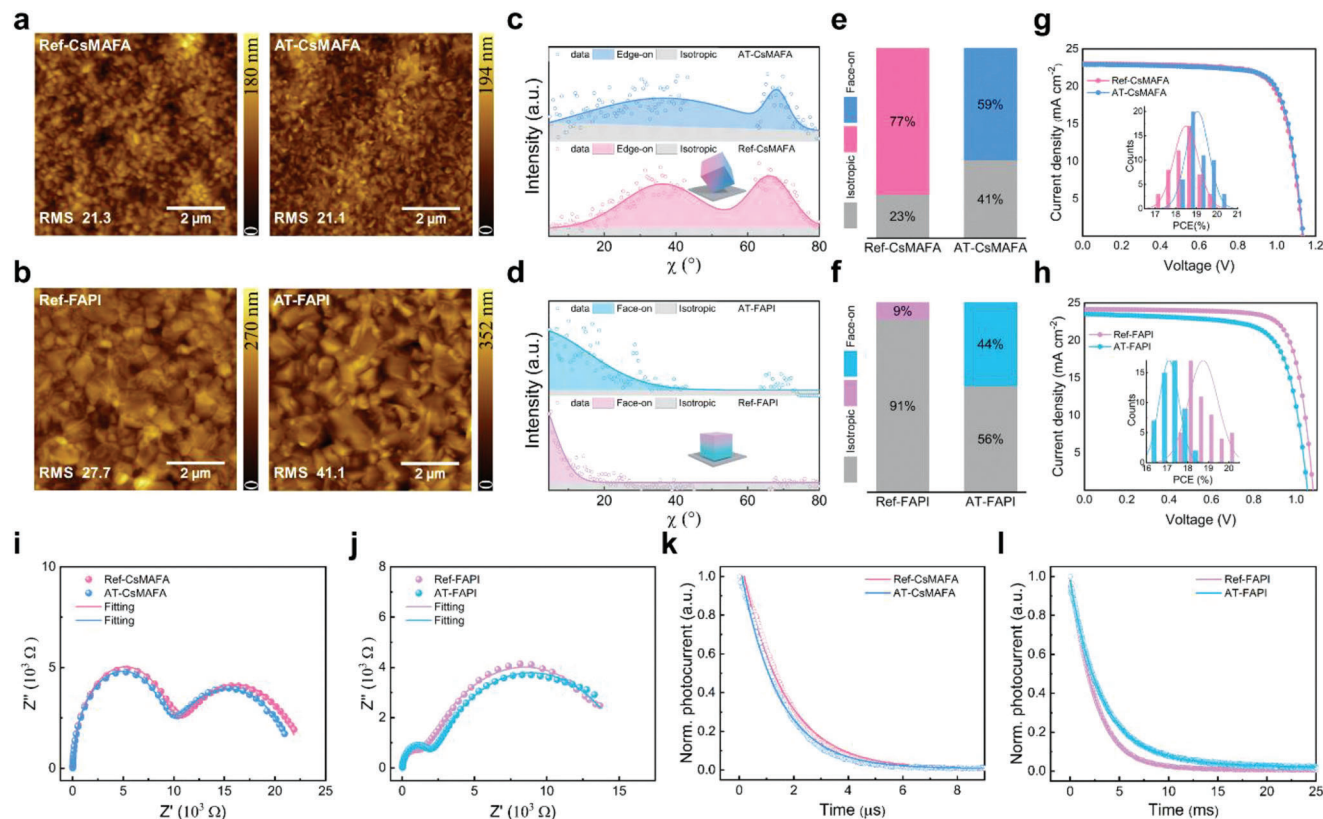
Figure 6. AFM images of Ref- and AT-thin films with a scale bar of 2 µm. a) CsMAFA, b) FAPI. Azimuthal tube cut data with fits (lines) of the (002/110) Bragg peak around $q = 1.00$ Å^{-1} extracted from 2D GIWAXS data, measured at $\alpha_i = 0.60°$. c) CsMAFA, d) FAPI. The edge-on and face-on orientations are illustrated by 3D model cubes. The relative material quantity (MQ) of each orientation. e) CsMAFA, f) FAPI. *J–V* curves of the champion devices measured under simulated AM 1.5G sunlight. g) CsMAFA, h) FAPI; inserted is the statistical distribution of PCE obtained from 50 cells from different batches. Nyquist plots of EIS of the Ref- and AT-devices. i) CsMAFA, j) FAPI. Transient photocurrent traces of Ref- and AT-devices. k) CsMAFA, l) FAPI.

the effect of direct annealing on the resulting film morphology gradually weakens with the increase of FA or Cs and MA ratio or Br and I ratio, especially in MAFA; and later, in CsMAFA and FAPI perovskite films. These results highlight the importance of the AT process in maintaining the integrity and continuity of polycrystalline thin films, with less sensitivity to the drip timing and drip rate of the anti-solvent. It also illustrates that the AT is an effective approach to obtain sufficiently high-quality thin films by finely controlling the crystallization kinetics.

2.6. Effect of AT on CsMAFA and FAPI Film Morphology and Device Performance

CsMAFA and FAPI are widely applied perovskite components in high-efficiency PSCs. Herein, we use CsMAFA and FAPI as light-absorbers to validate whether the AT is universal in optimizing film morphology and device photovoltaic performance of a wider variety of perovskite components. The SEM images (Figure S34a,b, Supporting Information) show no discernible difference in film morphology between Ref- and AT-CsMAFA films as well as Ref- and AT-FAPI films. This finding is consistent with previous work that increasing the ratio of FA, Br, and Cs in the perovskite component could also promote the formation

of full-coverage films in the absence of AT. However, the AFM shows diametrically opposite results for the film surface roughness of both perovskite components. The roughness (RMS) of CsMAFA films follows the same trend seen in the case of MAPI- and MAFA-films, decreasing from 21.3 nm for the Ref-film to 21.1 nm for the AT-film (**Figure 6**a). In contrast, the roughness of the AT-FAPI film shows an obvious increase from 27.7 to 41.1 nm (Figure 6b). As seen, with further increasing the FA or Br content, the negative effect of direct annealing on the film morphology gradually weakens and shows a positive influence on the crystal structure of FAPI films from the suppressed PbI$_2$ phase (Figure S35b, Supporting Information).

From the line profiles (Figure 6c) extracted from the 2D GIWAXS data (Figure S36, Supporting Information, white ring), the Ref-CsMAFA films show a pronounced crystal structure with an edge-on orientation at $\chi = 35°$ and $67°$. In contrast, the Bragg peaks in the case of AT-CsMAFA film are weaker and broadly distributed at $\chi = 35°$ and $68°$, suggesting that the proportion of edge-on oriented crystallites decreases, as obtained from the fraction of edge-on and isotropically oriented crystallites (Figure 6e), extracted from the Lorentz-corrected pole figure (Figure S37, Supporting Information). The proportion of edge-on oriented CsMAFA crystallites decreases from 77% to 59%, accompanied by an increased isotropic orientation MQ$_{iso}$ from 23% to 41% with

**ADVANCED
SCIENCE NEWS**

www.advancedsciencenews.com

**ADVANCED
MATERIALS**

www.advmat.de

the AT process. In the case of FAPI component, both films show a well-ordered face-on orientation from the strong scattering intensity at $\chi = 0°$ (Figure 6d). The relative material quality MQ of face-on oriented FAPI crystallites increases from 9% to 44%, and the isotropic orientation MQ_{iso} decreases from 91% to 56% with the AT process (Figure 6f). Combined with the previous analysis on MAPI and MAFA phase orientation, our finding shows that the influence of AT on the crystal orientation strongly depends on the perovskite composition. For different perovskite components, the AT reflects the difference and diversity in the crystal stacking pattern.

The champion *J–V* characteristics and the PCE statistical distribution of CsMAFA- and FAPI-devices extracted from different batches are shown in Figure 6g,h. The statistical distributions of other device parameters are plotted in Figures S38 and S39, Supporting Information, respectively, with the detailed values listed in Table S11, Supporting Information. Compared with the Ref-CsMAFA devices (the highest PCE is 20%, the average PCE is 18.5%), the AT-CsMAFA devices show a higher champion efficiency (20.2%) and an improved average efficiency (19.1%), as well as better reproducibility from the narrower distribution (Figure 6g, inset). However, the highest PCE for FAPI-devices decreases from 20.4% to 18.0%, accompanied by a decline in the average FF (from 0.75 to 0.70) with the AT process. The *J–V* photovoltaic parameters of CsMAFA and FAPI devices from the same batch are plotted in Figures S40 and S41, Supporting Information, respectively. The detailed values are listed in Table S12, Supporting Information. As seen, a similar improvement is also observed in the photovoltaic performance of devices from the same batch (Table S12, Supporting Information). The steady-state photocurrent density tracked at the maximum power point (Figure S42, Supporting Information) shows that the Ref-CsMAFA device undergoes a sharp performance drop under AM 1.5G illuminating for 300 s under air condition, and a minor difference occurs in both FAPI-devices that stabilize around 23.20 mA cm^{-2}. The dark *J–V* curves (Figure S43, Supporting Information) also show that the AT-CsMAFA device exhibits a lower trap density; while, the same improvement is not achieved in the AT-FAPI device. A similar phenomenon is observed from the TRPL measurements on thin films (Figures S44 and S45, Supporting Information). Compared with the reference, the smaller non-radiative recombination coefficient extracted from the AT-CsMAFA thin film suggests a smaller trap density (Table S13, Supporting Information). However, this improvement is not observed in the AT-FAPI thin film. The EIS results (Figure 6i,j; Table S6, Supporting Information) show facilitated charge carrier extraction and transfer at the interfaces and suppressed interface recombination in AT-CsMAFA and Ref-FAPI devices. Moreover, the reduced lifetime τ_t and the prolonged lifetime τ_r derived from TPC and TPV decay data (Figure 6k,l; Figure S46, Supporting Information) also suggest suppressed charge carrier recombination in AT-CsMAFA and Ref-FAPI devices (Tables S7 and S8, Supporting Information).[34] These results match well with the improved photovoltaic performance of devices (Table S11, Supporting Information).

Based on the above discussion, we find that the AT process has a positive effect on CsMAFA-films and corresponding device performance as MAPI and MAFA components. However, we cannot achieve the desired improvement in the surface rough-ness, charge carrier kinetics, and resulting device performance of AT-FAPI films and devices. We owe this phenomenon to the fact that the high FA component reaches the crystallization stage earlier than the MAPI component. In the FA-dominated component, the volatile MA is substantially replaced by FA, which reduces the amount of residual solvent and the loss of nucleated species. The crystallization behavior is already triggered upon anti-solvent dripping. Therefore, direct annealing has a minor influence on the crystal growth, but the AT process drives the preferential growth of crystals distributed in the surroundings prior to the middle due to the difference in the residual solvent diffusion rate in different regions (the solvent is not from the complex-solvent). This behavior triggers localized inhomogeneous crystallization, resulting in differences in film quality of the central and surrounding regions, and the devices suffer from a wide distribution of photovoltaic performance. This assumption is confirmed by the observed small white spherical and dendritic crystalline textures at the bottom and periphery of the aged films, whereas the upper interface is dark and translucent (Figure S47, Supporting Information). The irregular crystal texture is detrimental to the device performance.[11] In this work, we conduct a systematic and in-depth study on the effect of the AT on the film morphology and device performance based on various perovskite components from MA-dominated to FA-dominated, including MAPI, MAFA, CsMAFA, FAPI, $MA_{1-x}FA_xPI$, and $MAPI_{1-x}Br_x$. In addition, we investigate the effect of the AT on the charge carrier kinetics (recombination, transport, extraction, and so on) of perovskite films and devices, as well as explain why the device performance is improved from the photophysics perspective. Further, we find that the AT strategy reflects diversity in the stacking pattern of the crystallites for different perovskite components by GIWAXS measurements. Thus, this work provides a more comprehensive dissection and new insights into the role of the AT on morphology and device performance optimization compared with previous works.[15]

3. Conclusion

We demonstrate the AT as a facile and practical method to prepare high-quality MAPI thin films and high-reproducibility MAPI devices. With the application of the AT process, we achieve uniform, pinhole-free, and fully-covered perovskite thin films, together with fewer defects and superior electronic properties. The average PCE based on 50 AT-MAPI devices increases from 15.7% to 18.2%. We further explore the underlying correlations among the film morphology, FA, and Br content with and without AT, and propose explanations for their influence mechanisms. Further, we emphasize that the AT process is applicable to the film morphology and device performance optimization for MAPI, MAFA, and CsMAFA perovskite components, but not for the FA-dominated components. We foresee aging treatment as one of the most promising methods for realizing highly efficient and reproducible PSCs toward commercialization in the future.

Supporting Information

Supporting Information is available from the Wiley Online Library or from the author.

Acknowledgements

Conflict of Interest

The authors declare no conflict of interest.

Data Availability Statement

The data that support the findings of this study are available from the corresponding author upon reasonable request.

Keywords

[1] H. Min, D. Y. Lee, J. Kim, G. Kim, K. S. Lee, J. Kim, M. J. Paik, Y. K. Kim, K. S. Kim, M. G. Kim, T. J. Shin, S. Il Seok, *Nature* **2021**, *598*, 444.

[2] L. N. Quan, F. P. García De Arquer, R. P. Sabatini, E. H. Sargent, *Adv. Mater.* **2018**, *30*, 1801996.

[3] X. Wang, M. Li, B. Zhang, H. Wang, Y. Zhao, B. Wang, *Org. Electron.* **2018**, *52*, 172.

[4] a) S. D. Stranks, R. L. Z. Hoye, D. Di, R. H. Friend, F. Deschler, *Adv. Mater.* **2019**, *31*, 1803336; b) S. D. Stranks, G. E. Eperon, G. Grancini, C. Menelaou, M. J. P. Alcocer, T. Leijtens, L. M. Herz, A. Petrozza, H. J. Snaith, *Science* **2013**, *342*, 341.

[5] W. A. Dunlap-Shohl, Y. Zhou, N. P. Padture, D. B. Mitzi, *Chem. Rev.* **2018**, *119*, 3193.

[6] A. Barrows, A. Pearson, C. Kwak, A. Dunbar, A. Buckley, D. Lidzey, *Stem Cells Int.* **2014**, *7*, 2944.

[7] K. Hwang, Y. Jung, Y. Heo, F. Scholes, S. Watkins, J. Subbiah, *Adv. Mater.* **2015**, *27*, 283.

[8] M. Liu, M. B. Johnston, H. J. Snaith, *Nature* **2013**, *501*, 395.

[9] a) S. Pratap, F. Babbe, N. S. Barchi, Z. Yuan, T. Luong, Z. Haber, T.-B. Song, J. L. Slack, C. V. Stan, N. Tamura, C. M. Sutter-Fella, P. Müller-Buschbaum, *Nat. Commun.* **2021**, *12*, 5624; b) A. D. Taylor, Q. Sun, K. P. Goetz, Q. An, T. Schramm, Y. Hofstetter, M. Litterst, F. Paulus, Y. Vaynzof, *Nat. Commun.* **2021**, *12*, 1; c) D. P. McMeekin, P. Holzhey, S. O. Fürer, S. P. Harvey, L. T. Schelhas, J. M. Ball, S. Mahesh, S. Seo, N. Hawkins, J. Lu, *Nat. Mater.* **2022**, 1; d) N. Li, X. Niu, L. Li, H. Wang, Z. Huang, Y. Zhang, Y. Chen, X. Zhang, C. Zhu, H. Zai, Y. Bai, S. Ma, H. Liu, X. Liu, Z. Guo, G. Liu, R. Fan, H. Chen, J. Wang, Y. Lun, X. Wang, J. Hong, H. Xie, D. S. Jakob, X. G. Xu, Q. Chen, H. Zhou, *Science* **2021**, *373*, 561.

[10] a) K. Wang, M. C. Tang, H. X. Dang, R. Munir, D. Barrit, M. De Bastiani, E. Aydin, D. M. Smilgies, S. De Wolf, A. Amassian, *Adv. Mater.* **2019**, *31*, 1808357; b) R. Munir, A. D. Sheikh, M. Abdelsamie, H. Hu, L. Yu, K. Zhao, T. Kim, O. E. Tall, R. Li, D.-M. Smilgies, A. Amassian, *Adv. Mater.* **2017**, *29*, 1604113.

[11] C. Liu, Y.-B. Cheng, Z. Ge, *Chem. Soc. Rev.* **2020**, *49*, 1653.

[12] S. Sanchez, X. Hua, N. Phung, U. Steiner, A. Abate, *Adv. Energy Mater.* **2018**, *8*, 1702915.

[13] X. Li, D. Bi, C. Yi, J.-D. Décoppet, J. Luo, S. M. Zakeeruddin, A. Hagfeldt, M. Grätzel, *Science* **2016**, *353*, 58.

[14] P. Zhao, B. J. Kim, X. Ren, D. G. Lee, G. J. Bang, J. B. Jeon, W. B. Kim, H. S. Jung, *Adv. Mater.* **2018**, *30*, 1802763.

[15] a) D. M. Sanni, Y. Chen, A. S. Yerramilli, E. Ntsoenzok, J. Asare, S. A. Adeniji, O. V. Oyelade, A. A. Fashina, T. L. Alford, *Mater. Renewable Sustainable Energy* **2019**, *8*, 3; b) Y. Yao, X. Zou, J. Cheng, D. Chen, C. Chang, T. Ling, H. Ren, *Crystals* **2019**, *9*, 151; c) R. Liu, Z. Li, C. Chen, Y. Rao, X. Sun, L. Wang, X. Wang, Z. Zhou, T. Jiu, X. Guo, *ACS Appl. Mater. Interfaces* **2020**, *12*, 35043.

[16] M. D. Mcgehee, *Nat. Mater.* **2014**, *13*, 845.

[17] M. A. Reus, L. K. Reb, A. F. Weinzierl, C. L. Weindl, R. Guo, T. Xiao, M. Schwartzkopf, A. Chumakov, S. V. Roth, P. Müller-Buschbaum, *Adv. Opt. Mater.* **2022**, *10*, 2102722.

[18] Y. Wu, Q. Wang, Y. Chen, W. Qiu, Q. Peng, *Energy Environ. Sci.* **2022**, *15*, 4700.

[19] H. Li, R. Zhang, Y. Li, Y. Li, H. Liu, J. Shi, H. Zhang, H. Wu, Y. Luo, D. Li, Y. Li, Q. Meng, *Adv. Energy Mater.* **2018**, *8*, 1802012.

[20] Q. Jiang, Y. Zhao, X. Zhang, X. Yang, Y. Chen, Z. Chu, Q. Ye, X. Li, Z. Yin, J. You, *Nat. Photonics* **2019**, *13*, 460.

[21] H. Tan, A. Jain, O. Voznyy, X. Lan, F. P. García De Arquer, J. Z. Fan, R. Quintero-Bermudez, M. Yuan, B. Zhang, Y. Zhao, F. Fan, P. Li, L. N. Quan, Y. Zhao, Z.-H. Lu, Z. Yang, S. Hoogland, E. H. Sargent, *Science* **2017**, *355*, 722.

[22] J. Chung, S. S. Shin, K. Hwang, G. Kim, K. W. Kim, W. Kim, B. S. Ma, Y.-K. Kim, T.-S. Kim, J. Seo, *Energy Environ. Sci.* **2020**, *13*, 4854.

[23] L. A. Muscarella, E. M. Hutter, S. Sanchez, C. D. Dieleman, T. J. Savenije, A. Hagfeldt, M. Saliba, B. Ehrler, *J. Phys. Chem. Lett.* **2019**, *10*, 6010.

[24] N. Aristidou, C. Eames, I. Sanchez-Molina, X. Bu, J. Kosco, M. S. Islam, S. A. Haque, *Nat. Commun.* **2017**, *8*, 15218.

[25] N. Pellet, P. Gao, G. Gregori, T.-Y. Yang, M. K. Nazeeruddin, J. Maier, M. Grätzel, *Angew. Chem.* **2014**, *126*, 3215.

[26] M. Yang, T. Zhang, P. Schulz, Z. Li, G. Li, D. H. Kim, N. Guo, J. J. Berry, K. Zhu, Y. Zhao, *Nat. Commun.* **2016**, *7*, 1.

[27] J. H. Noh, S. H. Im, J. H. Heo, T. N. Mandal, S. I. Seok, *Nano Lett.* **2013**, *13*, 1764.

[28] a) Y. Lin, Y. Fang, J. Zhao, Y. Shao, S. J. Stuard, M. M. Nahid, H. Ade, Q. Wang, J. E. Shield, N. Zhou, *Nat. Commun.* **2019**, *10*, 1; b) S. Chen, X. Xiao, B. Chen, L. L. Kelly, J. Zhao, Y. Lin, M. F. Toney, J. Huang, *Sci. Adv.* **2021**, *7*, eabb2412.

[29] X. Cao, L. Zhi, Y. Li, F. Fang, X. Cui, L. Ci, K. Ding, J. Wei, *ACS Appl. Energy Mater.* **2018**, *1*, 868.

[30] a) A. Dubey, N. Kantack, N. Adhikari, K. M. Reza, S. Venkatesan, M. Kumar, D. Khatiwada, S. Darling, Q. Qiao, *J. Mater. Chem. A* **2016**,

4, 10231; b) B. Yang, O. Dyck, J. Poplawsky, J. Keum, A. Puretzky, S. Das, I. Ivanov, C. Rouleau, G. Duscher, D. Geohegan, K. Xiao, *J. Am. Chem. Soc.* **2015**, *137*, 9210.

[31] A. Z. Chen, M. Shiu, X. Deng, M. Mahmoud, D. Zhang, B. J. Foley, S.-H. Lee, G. Giri, J. J. Choi, *Chem. Mater.* **2019**, *31*, 1336.

[32] S. J. Yoon, K. G. Stamplecoskie, P. V. Kamat, *J. Phys. Chem. Lett.* **2016**, *7*, 1368.

[33] a) M. Saliba, T. Matsui, J.-Y. Seo, K. Domanski, J.-P. Correa-Baena, M. K. Nazeeruddin, S. M. Zakeeruddin, W. Tress, A. Abate, A. Hagfeldt, *Energy Environ. Sci.* **2016**, *9*, 1989. b) C. Yi, J. Luo, S. Meloni, A. Boziki, N. Ashari-Astani, C. Grätzel, S. M. Zakeeruddin, U. Röthlisberger, M. Grätzel, *Energy Environ. Sci.* **2016**, *9*, 656.

[34] Z. Xiong, X. Chen, B. Zhang, G. O. Odunmbaku, Z. Ou, B. Guo, K. Yang, Z. Kan, S. Lu, S. Chen, N. A. N. Ouedraogo, Y. Cho, C. Yang, J. Chen, K. Sun, *Adv. Mater.* **2022**, *34*, 2106118.